Design Optimization of Silicon and Lithium Niobate Hybrid Integrated Traveling-Wave Mach-Zehnder Modulator

Junming Cai, Changjian Guo, Chao Lu, Alan Pak Tao Lau, Pengxin Chen, and Liu Liu

***Abstract*—Lithium niobate, due to its strong electro-optic effect, is an excellent material for high-performance optical modulators. Hybrid integration of thin film lithium niobate and silicon photonic circuits makes it possible to fully exploit potentials of the two material systems. In this paper, we introduce a detailed design procedure for silicon and lithium niobate hybrid integrated modulator using coplanar line electrodes based on Mach-Zehnder interferometer push-pull configuration. A multiphysics model for the crossing section of the modulation section is proposed and analyzed. The results show that optimizing solely the $V_\pi L$ product would not lead to the best 3-dB bandwidth for a certain half-wave voltage due to the increased microwave losses. There exists an optimal ground-signal electrode gap value, which is about 8–9 μm for the present modulator structure. For these optimized structures, 3-dB bandwidths can reach 45 GHz and 137 GHz with half-wave voltages of 2 V and 4 V, respectively, for a lithium niobate waveguide total thickness of 600 nm and a ridge height of 200 nm.**

***Index Terms*—Lithium niobate, hybride Mach-Zehnder modulator.**

I. Introduction

INTEGRATED optical modulator is one of the most important devices in optical communications, which converts the information from the electrical signal to the optical carrier. Its performances, such as driving voltage, bandwidth, etc., directly affect the speed and power consumption of a communication system [1]. There exists many different platforms to realize an optical modulator, e.g. silicon-on-insulator (SOI) [2], indium phosphide [3], lithium niobate (LN) [1], [4]–[8], and electro-optic (EO) polymer [9] based on different types of structures, e.g. Mach-Zehnder interferometer (MZI) [1], [4], [6], [10], micro-resonator [6], [8]. Among them, the LN based EO modulator is probably the most matured type due to the large Pockels coefficient, the fast EO response, and the low optical loss of the LN material [4]–[7], [11]–[13]. Conventional MZI based traveling-wave (TW) EO modulator made of bulk LN has been widely used in optical communication systems for several decades [12]. Recently, a novel integration platform, i.e., thin film LN or LN on insulator (LNOI), has emerged and drawn many interests. Optical modulators based on etched ridge waveguides on thin-film LN exhibits excellent performances of small footprint, low driving voltage, and high bandwidth beyond 100 GHz [1], [4], [5], [7], [13]. On the other hand, as compared to other integration platforms, such as SOI, thin-film LN is still immature for photonic devices other than optical modulators. Non-vertical etched waveguide sidewalls from the current fabrication technology would also complicate the designs of passive devices based on the thin film LN [14]. Even for a simple bent waveguide, the anisotropy of the LN material would render an unexpected polarization coupling [15]. One solution to this difficulty is to use the hybrid integration technology [4]. In this case, the modulation sections, where only straight waveguides are needed, still rely on the thin film LN waveguide. The light can be coupled between the LN and silicon waveguides with a low loss (-0.42dB) using vertical adiabatic couplers [4]. Yet, other optical functional devices, e.g. splitters and routing waveguides, can be fabricated on other matured material platforms, such as SOI or silicon nitride [4], [5], [7], [8], [10], [16]. This type of hybrid integrated modulators has been demonstrated with even better performances, e.g., more stable operating point control, as compared to the ones on monolithic LNOI [17].

In order to fully exploit its potential, we systematically investigate the modulation performances of an MZI modulator based on the SOI/LN hybrid integration in this paper. The properties of the optical and microwave waveguides are modeled rigorously using a finite element based numerical solver (COMSOL). A common design procedure is proposed for all the structural

Manuscript received April 8, 2021; revised June 13, 2021; accepted June 16, 2021. Date of publication June 21, 2021; date of current version July 8, 2021. This work was supported in part by the National Key Research and Development Program under Grant 2019YFB1803902, in part by Guangdong Basic and Applied Basic Research Foundation under Grant 2021A1515012215, in part by the Science and Technology Planning Project of Guangdong Province under Grant 2019A050510039, and in part by the Natural Science Foundation of Guangdong Province under Grant 2018A0303130117. *(Corresponding authors: Pengxin Chen; Liu Liu.)*

Junming Cai, Changjian Guo, and Pengxin Chen are with the Centre for Optical and Electromagnetic Research, Guangdong Provincial Key Laboratory of Optical Information Materials and Technology, South China Academy of Advanced Optoelectronics, South China Normal University, Higher-Education Mega-Center, Guangzhou 510006, China (e-mail: junming.cai@coer-scnu.org; chenpx@m.scnu.edu.cn).

Chao Lu is with the Photonics Research Center, Department of Electronic and Information Engineering, Hong Kong Polytechnic University, Hong Kong SAR, China (e-mail: changjian.guo@coer-scnu.org; enluchao@polyu.edu.hk).

Alan Pak Tao Lau is with the Photonics Research Center, Department of Electrical Engineering, Hong Kong Polytechnic University, Hong Kong SAR, China (e-mail: eeaptlau@polyu.edu.hk).

Liu Liu is with the State Key Laboratory for Modern Optical Instrumentation, Centre for Optical & Electromagnetic Research, College of Optical Science and Engineering, International Research Center for Advanced Photonics, Zhejiang University, Hangzhou 310058, China (e-mail: liuliuopt@zju.edu.cn).

Digital Object Identifier 10.1109/JPHOT.2021.3090768

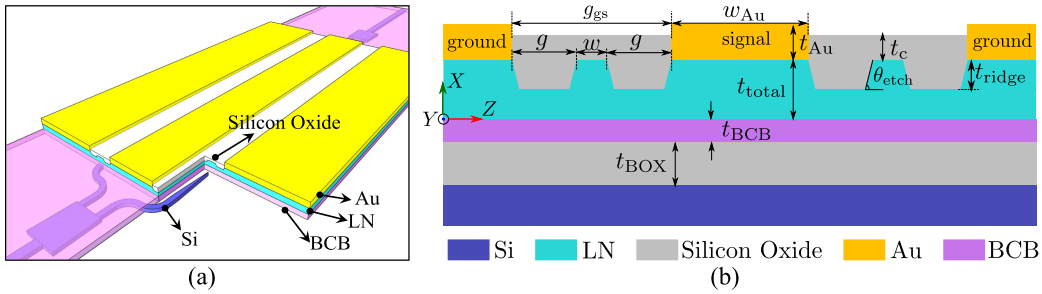

Fig. 1. (a) 3D schematic structure of the Si/LN hybrid integrated modulator. (b) Cross-sectional structure of the modulation section.

parameters in the modulation section. These parameters are further optimized for minimizing the driving voltage of the modulator while maintaining a large modulation bandwidth.

II. Design Method

The structure of the SOI/LN hybrid integrated modulator is sketched in Fig. 1(a). In this device, Si circuits are fabricated using standard complementary metal oxide semiconductor (CMOS) technology for Si photonics. An LN thin film is then transferred on the SOI chip using, e.g., adhesive bonding technology with the aid of a thin benzocyclobutene (BCB, Dow Chemical) layer. LN waveguides for the two arms of the MZI are subsequently patterned. A silicon oxide over-cladding layer is deposited and vias are opened through it at positions of the TW electrodes, which are deposited in the final step of the whole device fabrication. The electrodes are made of gold (Au) for its high electric conductivity and stability. Since the EO performance of the modulator depends on the cross-sectional structure of the modulation section, which is shown in Fig. 1(b), the optimization of these structural parameters will be discussed in this paper. The designs of the SOI circuits and the evanescent coupling structures are trivial and have been discussed in Ref. [4]. Therefore, they are not covered here.

The modulation section of the device is arranged in a TW fashion, where the driving radio frequency (RF) wave is propagating in the coplanar line waveguide (CPW) formed by three electrodes (ground-signal-ground, GSG), and the optical waves are propagating in the two LN ridge waveguides sitting between the electrodes in the same direction. The Z axis of the LN thin film, along which the EO coefficient of the material is the highest ($\gamma_{33} = 30\,pm/V$), lies within the chip surface plane and perpendicular to the propagation direction of the optical and RF waves. Once a voltage is applied on the signal electrode, the induced electrical field between the ground and signal electrodes will change the refractive index of the LN material, as well as the effective refractive index of the optical mode propagating in it. For the best EO interaction, the transverse electric (TE) mode with the major electrical field along the Z axis is considered here. Since the electrical fields in the two electrode gaps would have an opposite sign, the effective refractive indices of the waveguide modes of the two MZI arms would also undergo opposite shifts, i.e., the modulator is working in a push-pull manner.

The EO frequency response $m(\omega)$ of such a TW EO MZI modulator described above can be expressed as [16]:

$$m(\omega) = \left| \frac{2Z_{\text{in}}}{Z_{\text{in}} + 50} \frac{(50 + Z_0)\, F_+ + (50 - Z_0)\, F_-}{(50 + Z_0)\, e^{\gamma_{\text{m}} L} + (50 - Z_0)\, e^{-\gamma_{\text{m}} L}} \right|^2, \tag{1}$$

where, $F_\pm = (1 - e^{\pm\gamma_{\text{m}} L - j\frac{\omega}{c_0} n_{\text{o}} L})/(\pm\gamma_{\text{m}} L - j\frac{\omega}{c_0} n_{\text{o}} L)$, ω is the angular frequency of the RF driving signal, Z_0 is the characteristic impedance of the CPW, $Z_{\text{in}} = Z_0 \frac{50 + Z_0 \tanh(\gamma_{\text{m}} L)}{Z_0 + 50 \tanh(\gamma_{\text{m}} L)}$ is the RF impedance of the device seen from the input, L is the length of the modulation section, and $\gamma_{\text{m}} = \alpha_{\text{m}} + j\frac{\omega}{c_0} n_{\text{m}}$ is the RF propagation constant. α_{m}, n_{m}, and n_{o} are the RF propagation loss, the RF effective refractive index, and the group index of the optical mode, respectively.

In order to extract the required parameters in Eq. (1), three physical models should be considered for the cross-sectional structure shown in Fig. 1(b). Firstly, the optical mode property should be analyzed, which would give the group index n_{o}, as well as the propagation loss of the optical mode. The wavelength of the optical wave is assumed $1.55\,\mu m$ throughout the paper. Secondly, the RF mode property should be analyzed. The RF propagation constant can then be obtained. The characteristic impedance Z_0 can also be extracted from the RF mode distributions [19]. Note that the RF mode property is frequency dependent. Thus, these analyses should be carried out at each RF frequency point interested. Thirdly, the electro-static field distribution at a certain driving voltage should be analyzed. Correspondingly, the refractive index distribution $n_z(y, z)$ of the LN material induced by the EO effect can then be computed and expressed as [19]:

$$n_z(y, z) = n_{\text{e}} - \frac{1}{2} n_{\text{e}}^3 \gamma_{33} E_z, \tag{2}$$

where, E_z is the electrical field at a certain spatial point along the Z axis, n_{e} is the extraordinary refractive index of LN. With this refractive index distribution, one can again calculate the effective refractive index of the optical mode. From this analysis, the static $V_\pi L$ product can be extracted accordingly. All the above physical models were solved numerically using finite-element based algorithms (COMSOL). The material properties used in the simulations are listed in Table 1. Material dispersions are considered, which is necessary to evaluate the group index of the optical mode. Silicon substrate of a high resistivity is assumed here to minimize RF losses. The buried oxide layer

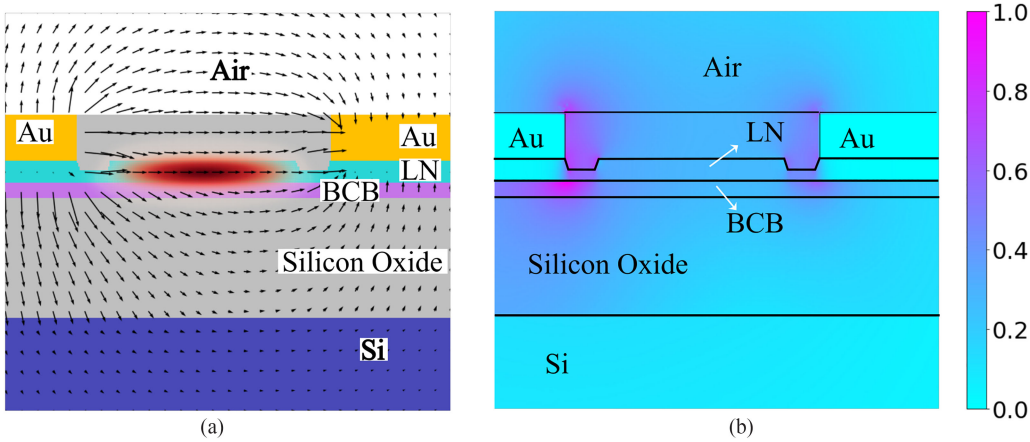

Fig. 2. (a) Typical distributions of the optical mode (colormap) and the static electrical field (vectors). (b) Typical distribution of the RF mode at 50 GHz.

has a thickness of 3 μm. These are typical specifications of an SOI structure from silicon photonics foundries. The BCB layer between the LN and the oxide is 370 nm, which is also a desired value from the adhesive bonding technology considering the coupling between the silicon and the LN waveguides [4]. The total thickness of the LN thin film t_{total} is fixed at 600 nm, which is optimal considering the mode confinement and the polarization mode hybridization [15]. Figure 2 shows typical distributions of the optical mode, the static electrical field, and the RF mode in the present structure.

III. Results

For optimizing the modulator structure, we aim at maximizing the bandwidth of the modulator at a certain V_π. Here, we do not put any constraint on the length of the device, which means that the $V_\pi L$ product is not necessarily minimal for an optimized structure. This is based on the fact that the state-of-the-art propagation loss of an LN ridge waveguide is about 0.027dB/cm [20]. A longer device is therefore affordable considering the insertion loss of the whole device.

The bandwidth of a TW modulator is mainly dominated by three factors, i.e., the RF loss α_{m} of the CPW, the characteristic impedance mismatch between the load, the CPW, and the generator, and the velocity mismatch (or the index difference) between the RF and optical propagating waves. In this paper, the impedances of the load and the generator are all assumed 50Ω as seen in Eq. (1). Ideally, the characteristic impedance Z_0 of the CPW should be matched to 50Ω as well, and the index difference $\Delta n = n_{\mathrm{m}} - n_{\mathrm{o}}$ should be 0. However, Z_0 and n_{m} are frequency dependent as mentioned above. It is almost impossible to achieve the perfect matching in the whole interested RF range. In the following analyses, we only consider one frequency point, i.e., at 50 GHz, for all the designs related to RF properties.

Firstly, the optical structure is designed. The angle of the LN waveguide θ_{etch} is assumed to 60°, which is adopted from the experimental data [4]. The GS electrode gap g_{gs} and the ridge depth of the LN waveguide t_{ridge} are arbitrarily chosen first. For each set of these parameters, the ridge width of the LN waveguide w can be optimized. We find that, within the parameter range considered throughout this paper, a wider w is always preferred, since it would give a better optical field confinement within the LN material, and hence a better $V_\pi L$ product. However, when further increasing w, the optical field would start seeing the metal electrodes, which would then increase the optical losses. This puts an upper limit for w. We set the tolerable optical loss here to be 0.01 dB/cm, which is already smaller than the state-of-the-art propagation loss of an LN ridge waveguide [20]. This also means that the metal induced losses would not be a limiting factor for the insertion loss of the whole device. The resulted maximum widths w_{max} are shown in Fig. 3(a). As expected, a deeper LN ridge depth and a wider GS electrode gap would support a wider LN waveguide. Figures 3(b) and 3(c) present the $V_\pi L$ products and optical group indices of the corresponding structures shown in Fig. 3(a). One can find that the $V_\pi L$ product almost exhibits a linear increase with respect to g_{gs}. Yet, it is not sensitive to t_{ridge}. Although a larger t_{ridge} would support a wider w_{max} according to Fig. 3(a), the optical confinement in the LN material tends to be similar for optimized structures at different t_{ridge}.

Next, one has to design the RF structure. Since g_{gs} is fixed, the characteristic impedance of the CPW is mainly related to the metal thickness t_{Au} and the width of the signal electrode w_{Au}. On the other hand, the RF losses of the CPW mainly includes metallic conductivity loss, dielectric loss, and radiation loss [21]. The radiation loss is related to the roughness of the Au electrode which can be neglected if the RF is below 200 GHz [22]. The dielectric loss and the metal conductivity loss are intrinsic properties of lossy materials, e.g., silicon oxide and Au, which is included already in the simulation model as shown in Tab. 1. In principle, the metal electrode should be thick enough to ensure that the skin effect of the metal under the RF field would not be limiting the RF loss. Here, a serial of simulations was carried out to find out the optimal metal thickness, and the results are shown in Fig. 4. One can find obviously that, for all the parameters considered here, the thicker the metal, the smaller the RF loss under impedance matching. Yet, the RF loss α_{m} decreases very quickly as the thickness of Au t_{Au} increases until 1.1 μm, which is about three times the skin depth of Au at 50 GHz. While

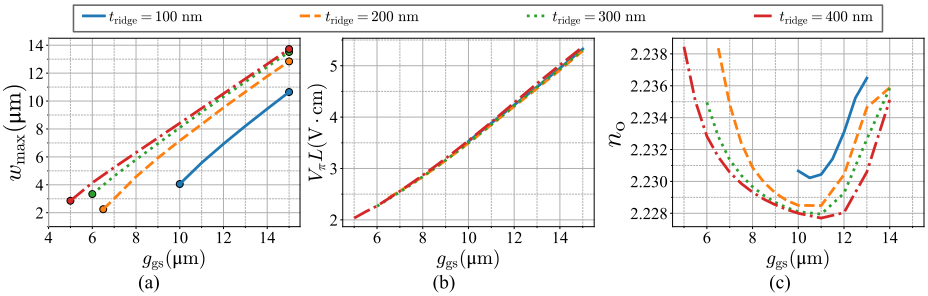

Fig. 3. (a) Maximum width of the LN ridge waveguide $w_{\max}$, (b) $V_\pi L$ product, and (c) optical group index with different GS gaps $g_{\rm gs}$ and ridge depths $t_{\rm ridge}$.

TABLE 1
MATERIAL PROPERTIES USED IN THE MODELLING

Property	Value
Relative permittivity of Si	11.9
Electrical conductivity of Si	0.01 S/m
Relative permittivity of SiO_2	$4 - 0.008j$
Refractive index of SiO_2*	$\sqrt{\frac{0.6961663\lambda^2}{\lambda^2 - 0.0684043^2} + \frac{0.4079426\lambda^2}{\lambda^2 - 0.1162414^2} + \frac{0.8974794\lambda^2}{\lambda^2 - 9.896161^2} + 1}$
Relative permittivity of LN [18]	$\epsilon_{r11}^T = \epsilon_{r22}^T = 85,\ \epsilon_{r33}^T = 29$
Refractive index of LN*	$n_{\rm o} = \sqrt{\frac{2.6734\lambda^2}{\lambda^2 - 0.01764} + \frac{1.2290\lambda^2}{\lambda^2 - 0.05914} + \frac{12.614\lambda^2}{\lambda^2 - 474.60} + 1}$ $n_{\rm e} = \sqrt{\frac{2.9804\lambda^2}{\lambda^2 - 0.02047} + \frac{0.5981\lambda^2}{\lambda^2 - 0.0666} + \frac{8.9543\lambda^2}{\lambda^2 - 416.08} + 1}$
Relative permittivity of BCB	$3.1 - 0.133j$
Refractive index of BCB	1.547
Relative permittivity of Au	1.0
Electrical conductivity of Au	4.1×10^7 S/m
Refractive index of Au*	$0.52406 + 10.742j$

* Data is from https://refractiveindex.info/; and λ is the optical wavelength in μm.

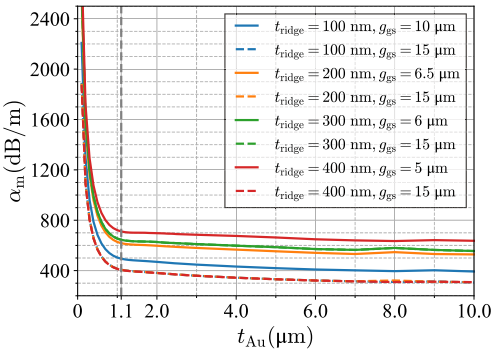

Fig. 4. RF loss $\alpha_{\rm m}$ versus the thickness of the metal electrode $t_{\rm Au}$ for different structural parameters under impedance matching. The vertical, gray-dotted line dictates the thickness of 1.1 μm.

this trend reached a plateau when $t_{\rm Au}$ is larger than 1.1 μm. Practically, a too thick metal will complicate the fabrication process, and increase the cost as well. Therefore, in the following analyses $t_{\rm Au}$ is fixed at 1.1 μm.

Once $t_{\rm Au}$ is fixed, the width of the signal electrode $w_{\rm Au}$ can then be designed for impedance match ($Z_0 = 50\,\Omega$). The thickness of the upper cladding SiO_2 $t_{\rm c}$ can also be designed to achieve the index match ($|\Delta n| \approx 0$). Note that variations in $t_{\rm c}$ would also affect slightly the characteristic impedance, and $w_{\rm Au}$ on the RF effective index as well. Therefore, these two parameters should be optimized together in principle. The results are shown in Fig. 5. Apparently, a larger $g_{\rm gs}$ would require a larger $w_{\rm Au}$ to achieve impedance matching. However, $t_{\rm ridge}$ would not largely affect the impedance. This is due to the structure considered in this paper, where only small trenches are etched beside the ridge to form the waveguide as shown in Fig. 1(b). As for the index matching, a thicker over cladding would be normally required for a narrower $g_{\rm gs}$ and a larger $t_{\rm ridge}$. Figure 5(c) presents the RF loss $\alpha_{\rm m}$ of each optimized structure. Apparently, a larger $g_{\rm gs}$ would give a smaller RF loss $\alpha_{\rm m}$.

So far, all the structural parameters have been optimized for each set of $g_{\rm gs}$ and $t_{\rm ridge}$ to achieve impedance and index matching, and to minimize the optical loss as well. Now we

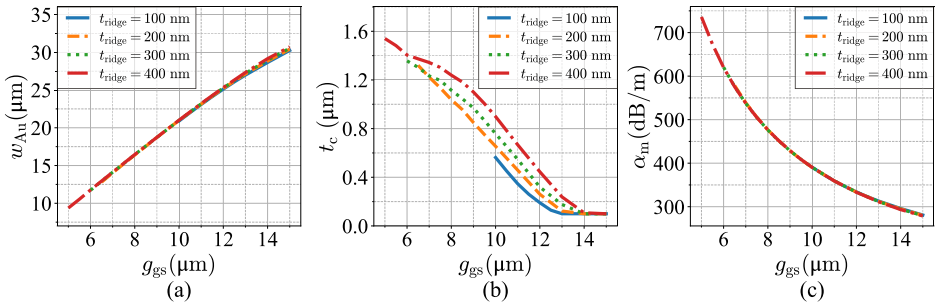

Fig. 5. Structural parameters of (a) w_{Au} and (b) t_{c} for achieving impedance and index mating at different g_{gs} and t_{ridge}. (c) Corresponding RF losses of the optimized structures in (a) and (b).

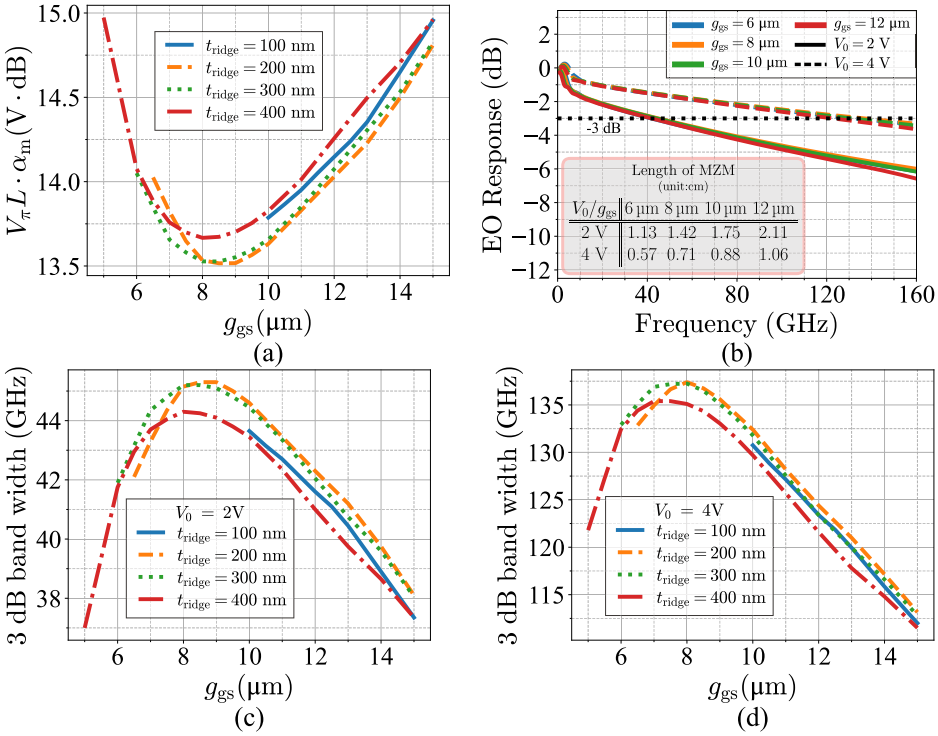

Fig. 6. (a) $V_\pi L \cdot \alpha_{\mathrm{m}}$ vs. g_{gs}. (b) EO responses for different g_{gs} and half-wave voltages. The lengths of the modulation section are marked in the inset. (c) and (d) 3-dB bandwidths vs. g_{gs}, when half-wave voltages are 2 V and 4 V, respectively.

can analyze how the modulation performances, such as driving voltages and bandwidths, would be affected by these structural parameters. Approximately, for a TW modulator under perfect impedance and index matching, the 3-dB bandwidth (B) and the length of modulation section (L_0) would have the following relation [23]:

$$B\left(L_0\alpha_{\mathrm{m}}\right)^2 = const. \tag{3}$$

Since L_0 is inverse proportional to the half-wave voltage V_0 of the modulator through the relation $L_0 = V_\pi L/V_0$, where the $V_\pi L$ product can be extracted from the electric field distributions for each structure as mentioned before, Eq. (3) can then be rewritten as:

$$B\left(V_\pi L \cdot \alpha_{\mathrm{m}}/V_0\right)^2 = const. \tag{4}$$

From the above equation, one can find that for a given V_0, the quantity $V_\pi L \cdot \alpha_{\mathrm{m}}$, which is shown in Fig. 6(a), has to be minimized in order to achieve the best bandwidth. From Fig. 6(a), one can find that $V_\pi L \cdot \alpha_{\mathrm{m}}$ exhibits a minimal point around $g_{\mathrm{gs}} = 8.5\,\mu m$ for t_{ridge} from 200 nm to 400 nm. For $t_{\mathrm{ridge}} = 100\,nm$, the etching depth of the LN ridge is too small to provide a sufficient lateral light confinement. In this case, the best g_{gs} is the smallest one to maintain a low optical loss, i.e., $< 0.01\,dB/cm$. From these analyses, we can already conclude that there exists an optimal GS electrode gap g_{gs} and the corresponding other structural parameters, i.e., w_{max}, w_{Au}, etc., for the present modulator to achieve the highest bandwidth at a certain half wave voltage V_0. Although a smaller g_{gs} would give a smaller $V_\pi L$ product, and intuitively it would help to increase the bandwidth since the device would become shorter, the increased RF loss, in this case, would actually prevent the overall bandwidth from the benefit of a short device.

Yet, the above results are still based on a semi-analytic approximation, i.e., Eq. (4). It is still necessary to investigate the

bandwidth performance of the optimized structures more accurately by directly using Eq. (1). Figure 6(b) presents the typical EO frequency response $m(\omega)$ when the half-wave voltage of a modulator is set to 2 V and 4 V, respectively. Clearly, the best frequency response is obtained when $g_{\rm gs} = 8$–$9\ \mu m$. Figures 6(c) and 6(d) further presents the 3-dB bandwidth (B), which can be extracted from the EO frequency response in, e.g., Fig. 6(b), with different $g_{\rm gs}$ and $t_{\rm ridge}$. For $V_0 = 4V$, the best 3-dB bandwidth reaches 137 GHz for $g_{\rm gs} \approx 8\,\mu m$ and $t_{\rm ridge} = 200\,nm$. For $V_0 = 2V$, the best 3-dB bandwidth reaches 45 GHz for $g_{\rm gs} \approx 9\,\mu m$ and $t_{\rm ridge} = 200\,nm$.

IV. Conclusion

In this paper, we have described a detailed design procedure for SOI/LN hybrid integrated EO modulator based on the MZI push-pull configuration. The cross section of the modulation section has been rigorously modeled using numerical algorithms with practical material parameters. The optical and RF mode properties were extracted accurately, which is essential for determining the modulation performances of the device. We started the design by choosing the electrode gap and ridge depth of the LN waveguide. Then, the width of the LN waveguide was determined by minimizing the $V_\pi L$ product while maintaining a low optical loss. The RF waveguide structure, including the metal thickness, the signal electrode width, and the thickness of the over-cladding oxide, was subsequently optimized to achieve the impedance and index matching. The 3-dB bandwidth of the designed modulator was calculated with a TW model.

The main conclusion of this paper is that there exists an optimal electrode gap $g_{\rm gs}$ value, which is around 8–9 μm for the present modulator structure, to achieve the best 3-dB bandwidth at a certain half-wave voltage. For this optimized structure, the width of the LN ridge waveguide is $> 4\,\mu m$, which is already in the multimode regime, and the $V_\pi L$ product is not necessarily the smallest in these cases. This is different from common practices [16]. The design discussed in this paper is rather conservative, as the metal induced loss was theoretically kept below 0.01 dB/cm. If higher optical losses are tolerable, the metal electrode can be put closer to the LN ridge waveguide, and hence a smaller $V_\pi L$ product can be obtained. Thus, a higher bandwidth should be achievable for the same half-wave voltage. Nevertheless, the same design procedure discussed here can be applied. The optimal electrode gap and LN waveguide width in these cases can be determined accordingly.

References

[1] C. Wang *et al.*, "Integrated lithium niobate electro-optic modulators operating at CMOS-compatible voltages," *Nature*, vol. 562, no. 7725, pp. 101–104, Oct. 2018, doi: 10.1038/s41586-018-0551-y.

[2] G. T. Reed, G. Mashanovich, F. Y. Gardes, and D. J. Thomson, "Silicon optical modulators," *Nature Photon.*, vol. 4, no. 8, pp. 518–526, 2010. [Online]. Available: https://doi.org/10.1038/nphoton.2010.179

[3] Y. Ogiso *et al.*, "Over 67 GHz bandwidth and 1.5 VV_π InP-based optical IQ modulator with n-i-p-n heterostructure," *J. Lightw. Technol.*, vol. 35, no. 8, pp. 1450–1455, 2017. [Online]. Available: http://jlt.osa.org/abstract.cfm?URI=jlt-35-8-1450

[4] M. He *et al.*, "High-performance hybrid silicon and lithium niobate Mach-Zehnder modulators for 100 Gbit s^{-1} and beyond," *Nature Photon.*, vol. 13, no. 5, pp. 359–364, 2019. [Online]. Available: https://doi.org/10.1038/s41566-019-0378-6

[5] P. O. Weigel *et al.*, "Bonded thin film lithium niobate modulator on a silicon photonics platform exceeding 100 GHz 3-dB electrical modulation bandwidth," *Opt. Exp.*, vol. 26, no. 18, pp. 23728–23739, 2018. [Online]. Available: http://www.opticsexpress.org/abstract.cfm?URI=oe-26-18-23728

[6] C. Wang, M. Zhang, B. Stern, M. Lipson, and M. Lončar, "Nanophotonic lithium niobate electro-optic modulators," *Opt. Exp.*, vol. 26, no. 2, pp. 1547–1555, 2018. [Online]. Available: http://www.opticsexpress.org/abstract.cfm?URI=oe-26-2-1547

[7] A. J. Mercante, P. Yao, S. Shi, G. Schneider, J. Murakowski, and D. W. Prather, "110 GHz CMOS compatible thin film modulator on silicon," *Opt. Exp.*, vol. 24, no. 14, pp. 15590–15595, 2016. [Online]. Available: http://www.opticsexpress.org/abstract.cfm?URI=oe-24-14-15590

[8] A. N. R. Ahmed, S. Shi, M. Zablocki, P. Yao, and D. W. Prather, "Tunable hybrid silicon nitride and thin-film lithium niobate electro-optic microresonator," *Opt. Lett.*, vol. 44, no. 3, pp. 618–621, 2019. [Online]. Available: http://ol.osa.org/abstract.cfm?URI=ol-44-3-618

[9] M. Lee *et al.*, "Broadband modulation of light by using an electro-optic polymer," *Science*, vol. 298, no. 5597, pp. 1401–1403, 2002. [Online]. Available: https://science.sciencemag.org/content/298/5597/1401

[10] A. N. R. Ahmed, S. Nelan, S. Shi, P. Yao, A. Mercante, and D. W. Prather, "Subvolt electro-optical modulator on thin-film lithium niobate and silicon nitride hybrid platform," *Opt. Lett.*, vol. 45, no. 5, pp. 1112–1115, 2020. [Online]. Available: http://ol.osa.org/abstract.cfm?URI=ol-45-5-1112

[11] A. Rao and S. Fathpour, "Compact lithium niobate electrooptic modulators," *IEEE J. Sel. Topics Quantum Electron.*, vol. 24, no. 4, pp. 1–14, Jul./Aug. 2018.

[12] E. L. Wooten *et al.*, "A review of lithium niobate modulators for fiber-optic communications systems," *IEEE J. Sel. Topics Quantum Electron.*, vol. 6, no. 1, pp. 69–82, Jan./Feb. 2000.

[13] A. J. Mercante, S. Shi, P. Yao, L. Xie, R. M. Weikle, and D. W. Prather, "Thin film lithium niobate electro-optic modulator with terahertz operating bandwidth," *Opt. Exp.*, vol. 26, no. 11, pp. 14810–14816, 2018. [Online]. Available: http://www.opticsexpress.org/abstract.cfm?URI=oe-26-11-14810

[14] H. Xu, D. Dai, L. Liu, and Y. Shi, "Proposal for an ultra-broadband polarization beam splitter using an anisotropy-engineered Mach-Zehnder interferometer on the x-cut lithium-niobate-on-insulator," *Opt. Exp.*, vol. 28, no. 8, pp. 10899–10908, 2020. [Online]. Available: http://www.opticsexpress.org/abstract.cfm?URI=oe-28-8-10899

[15] J. Wang, P. Chen, D. Dai, and L. Liu, "Polarization coupling of X-cut thin film lithium niobate based waveguides," *IEEE Photon. J.*, vol. 12, no. 3, Jun. 2020, Art. no. 2200310.

[16] P. O. Weigel, F. Valdez, J. Zhao, H. Li, and S. Mookherjea, "Design of high-bandwidth, low-voltage and low-loss hybrid lithium niobate electro-optic modulators," *J. Physics: Photon.*, vol. 3, no. 1, Nov. 2020, Art. no. 012001. doi: 10.1088/2515-7647/abc17e

[17] S. Sun *et al.*, "Bias-drift-free Mach-Zehnder modulators based on a heterogeneous silicon and lithium niobate platform," *Photon. Res.*, vol. 8, no. 12, pp. 1958–1963, 2020. [Online]. Available: http://www.osapublishing.org/prj/abstract.cfm?URI=prj-8-12-1958

[18] R. S. Weis and T. K. Gaylord, "Lithium niobate: Summary of physical properties and crystal structure," *Appl. Phys. A*, vol. 37, no. 4, pp. 191–203, 1985. [Online]. Available: https://doi.org/10.1007/BF00614817

[19] G. Ghione, *Semiconductor Devices for High-Speed Optoelectronics*, 1st ed. New York, NY, USA: Cambridge Univ. Press, pp. 356–439, 2009.

[20] R. Wu *et al.*, "Long low-loss-litium niobate on insulator waveguides with sub-nanometer surface roughness," *Nanomater.*, vol. 8, no. 11, Nov. 2018, Art. no. 910. [Online]. Available: https://www.mdpi.com/2079-4991/8/11/910

[21] A. Honardoost, R. Safian, A. Rao, and S. Fathpour, "High-speed modeling of ultracompact electrooptic modulators," *J. Lightw. Technol.*, vol. 36, no. 24, pp. 5893–5902, 2018. [Online]. Available: http://jlt.osa.org/abstract.cfm?URI=jlt-36-24-5893

[22] M. Y. Frankel, S. Gupta, J. A. Valdmanis, and G. A. Mourou, "Terahertz attenuation and dispersion characteristics of coplanar transmission lines," *IEEE Trans. Microw. Theory Techn.*, vol. 39, no. 6, pp. 910–916, Jun. 1991.

[23] A. Chowdhury and L. McCaughan, "Figure of merit for near-velocity-matched traveling-wave modulators," *Opt. Lett.*, vol. 26, no. 17, pp. 1317–1319, 2001. [Online]. Available: http://ol.osa.org/abstract.cfm?URI=ol-26-17-1317